CARBON CYCLE

Strong Southern Ocean carbon uptake evident in airborne observations

Matthew C. Long[1]*, Britton B. Stephens[1], Kathryn McKain[2,3], Colm Sweeney[3], Ralph F. Keeling[4], Eric A. Kort[5], Eric J. Morgan[4], Jonathan D. Bent[1,4]†, Naveen Chandra[6]‡, Frederic Chevallier[7], Róisín Commane[8], Bruce C. Daube[9], Paul B. Krummel[10], Zoë Loh[10], Ingrid T. Luijkx[11], David Munro[2,3], Prabir Patra[12], Wouter Peters[11,13], Michel Ramonet[7], Christian Rödenbeck[14], Ann Stavert[10], Pieter Tans[3], Steven C. Wofsy[9,15]

The Southern Ocean plays an important role in determining atmospheric carbon dioxide (CO_2), yet estimates of air-sea CO_2 flux for the region diverge widely. In this study, we constrained Southern Ocean air-sea CO_2 exchange by relating fluxes to horizontal and vertical CO_2 gradients in atmospheric transport models and applying atmospheric observations of these gradients to estimate fluxes. Aircraft-based measurements of the vertical atmospheric CO_2 gradient provide robust flux constraints. We found an annual mean flux of −0.53 ± 0.23 petagrams of carbon per year (net uptake) south of 45°S during the period 2009–2018. This is consistent with the mean of atmospheric inversion estimates and surface-ocean partial pressure of CO_2 (P_{CO_2})–based products, but our data indicate stronger annual mean uptake than suggested by recent interpretations of profiling float observations.

Ocean water-column carbon inventories suggest that the Southern Ocean accounts for more than 40% of the cumulative global ocean uptake of anthropogenic CO_2 (*1*, *2*). However, estimates of contemporary net Southern Ocean air-sea carbon fluxes based on surface-ocean partial pressure of CO_2 (P_{CO_2}) observations or atmospheric inversions remain highly uncertain (*3*–*8*). Recent interpretations of profiling float observations have introduced further complications, proposing a profound revision of the Southern Ocean carbon budget, with reduced summertime uptake and larger wintertime outgassing (*9*, *10*). Given the Southern Ocean's critical role as a sink for anthropogenic CO_2, as well as indications that regional fluxes vary substantially on decadal time scales (*7*, *11*, *12*), it is essential to develop more-robust constraints on Southern Ocean air-sea CO_2 exchange. Observations of atmospheric CO_2 provide an opportunity for doing so, as the atmosphere effectively integrates flux signals over large surface regions. Atmospheric inversion models provide a formal statistical method to estimate fluxes that optimally satisfy atmospheric observational constraints, given circulation simulated by data-constrained atmospheric transport models (*4*, *13*, *14*). However, global-scale atmospheric inversion models have not converged on consistent Southern Ocean fluxes, as they suffer from inaccuracies in the simulated transport, reliance on uncertain "prior" flux estimates, and requirements to meet tighter constraints elsewhere in the world, where signals are stronger and measurements less sparse (*4*, *13*–*17*).

In this study, we derived "emergent constraints" on regional air-sea fluxes by relating fluxes in a collection of models to observable gradients in CO_2 in the atmosphere directly overlying the Southern Ocean. We used observations from nine deployments of three recent aircraft projects: the HIAPER Pole-to-Pole Observations (HIPPO) project (*18*), the O_2/N_2 Ratio and CO_2 Airborne Southern Ocean (ORCAS) study (*19*), and the Atmospheric Tomography (ATom) mission (*20*) (see supplementary materials, hereafter SM). We also examined 44 atmospheric CO_2 records from surface monitoring stations in the high-latitude Southern Hemisphere, selecting and filtering the highest-quality data (SM). Collectively, these observations show a distinct pattern in the seasonal variability of atmospheric CO_2 overlying the Southern Ocean, most notably characterized by lower-troposphere CO_2 depletion in austral summer and neutral to weakly positive enhancement in austral winter (Figs. 1 and 2, A to C). To isolate CO_2 gradients driven by Southern Ocean fluxes, we examined CO_2 anomalies relative to a local reference, using potential temperature (θ) to delineate boundaries in the vertical dimension (SM). We defined a metric quantifying the vertical CO_2 gradient, $\Delta_\theta CO_2$, as the difference between the median value of CO_2 observed south of 45°S, where $\theta < 280$ K, and that in the mid- to upper-troposphere, where $295\ K < \theta < 305\ K$. The aircraft observations suggest that the amplitude of seasonal variation in CO_2 is minimized within this upper θ range relative to the rest of the column (fig. S7); it is also above the vertical extent of wintertime, near-surface homogeneity (Fig. 2A) and below altitudes substantially influenced by the stratosphere, making it a good reference for detecting regional air-sea flux signals (see SM). Similarly, we defined a metric of the horizontal surface gradient, $\Delta_y CO_2$, as the difference between CO_2 averaged across stations in the core latitudes of summertime CO_2 drawdown (Fig. 1, C and D, shaded region) and that at the South Pole Observatory (SPO). $\Delta_\theta CO_2$ is strongly negative in the austral summer, followed by near-neutral conditions in the austral winter through spring (Fig. 2B). Correspondingly, $\Delta_y CO_2$ also indicates summertime drawdown at the surface and weakly positive to near-neutral conditions in winter (Fig. 2C), although the amplitude of seasonal variation in $\Delta_\theta CO_2$ is more than three times larger than that in $\Delta_y CO_2$. Variation in drawdown intensity across stations contributing to $\Delta_y CO_2$ likely reflects differential sampling of air exposed to strong ocean productivity signals (fig. S4).

We developed inferences about air-sea CO_2 fluxes from these gradient metrics by examining a collection of atmospheric inverse models that simulate time-varying, three-dimensional CO_2 fields sampled to replicate observations (SM). The inverse models demonstrate that seasonality in $\Delta_\theta CO_2$ and $\Delta_y CO_2$ is dominated by Southern Ocean air-sea fluxes. Although land and fossil fuel fluxes are small south of 45°S, extraregional contributions do influence local gradients via transport from the north. The models explicitly simulate CO_2 tracers responsive only to ocean (CO_2^{ocn}), land (CO_2^{lnd}), and fossil fuel (CO_2^{ff}) fluxes and subject to identical transport fields. The simulations of these tracers indicate that the influence of land fluxes generally opposes the effect of fossil fuel emissions for both gradient metrics, and the seasonality in the land and fossil fuel tracers is much weaker than the ocean-derived signal (Fig. 2, D and E, and fig. S6). The negative vertical (positive horizontal) gradient in fossil fuel CO_2 is consistent with elevated CO_2 concentrations in the equatorward portion of the

[1]National Center for Atmospheric Research, Boulder, CO, USA. [2]Cooperative Institute for Research in Environmental Sciences, University of Colorado, Boulder, CO, USA. [3]Global Monitoring Laboratory, National Oceanic and Atmospheric Administration, Boulder, CO, USA. [4]Scripps Institution of Oceanography, University of California, San Diego, La Jolla, CA, USA. [5]Department of Climate and Space Sciences and Engineering, University of Michigan, Ann Arbor, MI, USA. [6]National Institute of Environmental Studies, Tsukuba, Japan. [7]Laboratoire des Sciences du Climat et de l'Environnement, IPSL-LSCE, CEA-CNRS-UVSQ, UMR8212 91191, France. [8]Department of Earth and Environmental Sciences, Lamont-Doherty Earth Observatory of Columbia University, Palisades, NY, USA. [9]Department of Earth and Planetary Sciences, Harvard University, Cambridge, MA, USA. [10]Climate Science Centre, CSIRO Oceans and Atmosphere, Aspendale, Victoria, Australia. [11]Department of Meteorology and Air Quality, Environmental Sciences Group, Wageningen University, Netherlands. [12]Research Institute for Global Change, Japan Agency for Marine-Earth Science and Technology (JAMSTEC), Yokohama, Japan. [13]Centre for Isotope Research, University of Groningen, Groningen, Netherlands. [14]Max Planck Institute for Biogeochemistry, Jena, Germany. [15]Harvard John A. Paulson School of Engineering and Applied Sciences, Harvard University, Cambridge, MA, USA.
*Corresponding author. Email: mclong@ucar.edu
†Present address: Picarro, Inc., Santa Clara, CA, USA.
‡Present address: Research Institute for Global Change, JAMSTEC, Yokohama, Japan.

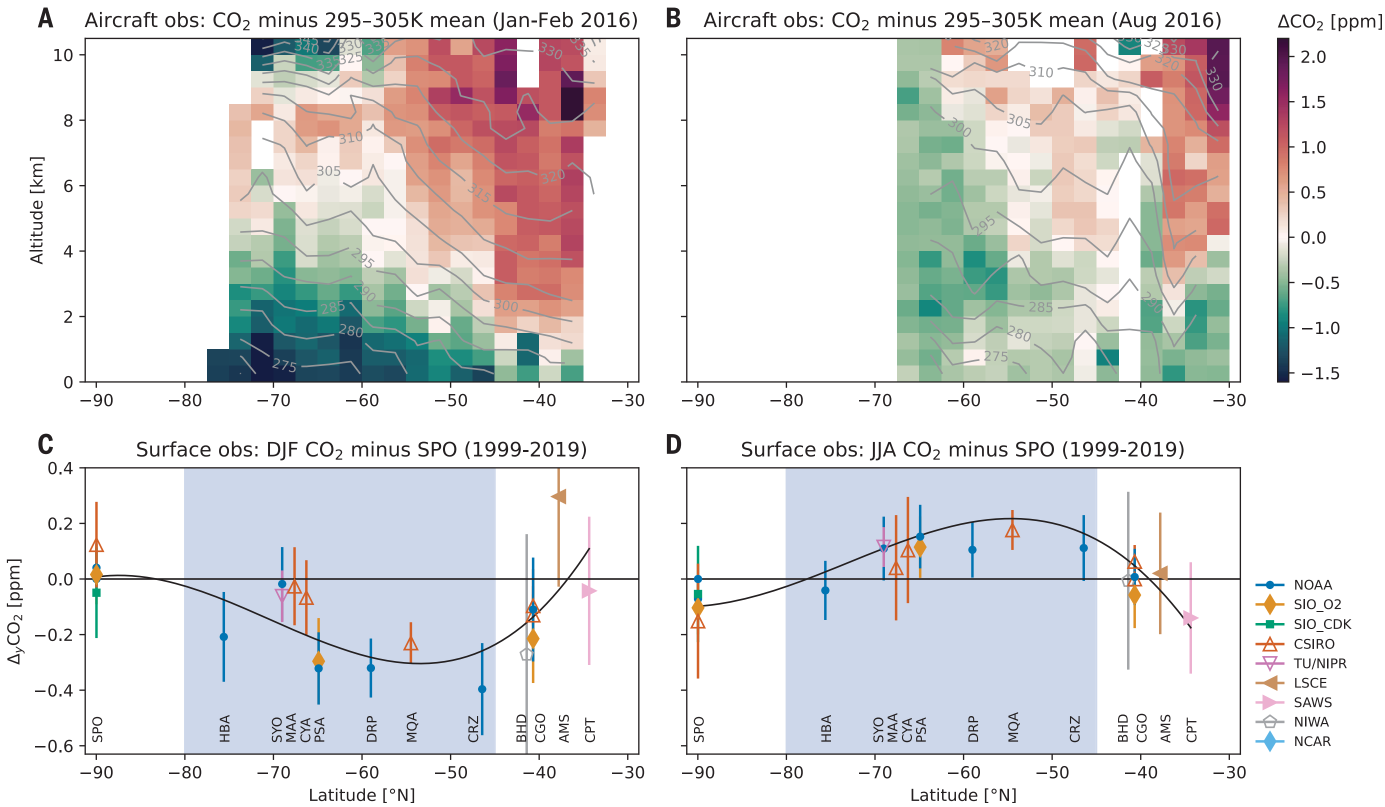

Fig. 1. Observed patterns in atmospheric CO_2 over the Southern Ocean. (**A** and **B**) Cross sections observed by aircraft during (A) ORCAS, in January to February 2016, and (B) ATom-1, in August 2016. Colors show the observed CO_2 dry air mole fraction relative to the average observed within the 295–305 K potential temperature range south of 45°S on each campaign. Contour lines show the observed potential temperature. See figs. S1 and S2 for flight tracks and cross-sectional plots for all campaigns, and figs. S3 and S4 for simulated fields. (**C** and **D**) Compilation of mean CO_2 observed at surface monitoring stations minus the National Oceanic and Atmospheric Administration (NOAA) in situ record at the South Pole Observatory (SPO) during the period 1999–2019 for (C) summer (DJF) and (D) winter (JJA). The black line is a spline fit provided simply as a visual guide. Blue shading denotes the latitude band in which we designate "Southern Ocean stations." See table S1 and fig. S5 for station locations and temporal coverage. SM includes additional methodological details.

domain, particularly at high altitude (Fig. 1, A and B, and figs. S2 to S4). Ancillary measurements of methane-mixing ratios confirm that this feature reflects long-range transport of emission signals from land, but that it has little influence on $\Delta_\theta CO_2$ (figs. S6 and S8). Additional evidence that fossil fuel emissions make only small contributions to the annual mean and seasonality in $\Delta_y CO_2$ comes from ancillary observations of sulfur hexafluoride—which provides an analog for fossil fuel CO_2 (*21*) and shows very little spatial or temporal structure over the Southern Ocean (fig. S9).

To develop quantitative flux estimates, we related simulated $\Delta_\theta CO_2^{ocn}$ and $\Delta_y CO_2^{ocn}$ to regionally integrated, temporally averaged air-sea flux in each modeling system (Fig. 3). In addition to inverse models, we included forward atmospheric transport integrations forced with spatially explicit surface-ocean P_{CO_2}-based flux datasets (SM). Ultimately, each model realization was a forward simulation producing three-dimensional CO_2 fields from which we computed gradient metrics consistent with the model's surface fluxes and atmospheric transport. The relationship between the fluxes and simulated gradient metrics across the collection of models enabled using the observed gradients to constrain Southern Ocean fluxes. We assumed that the relevant surface-influence region can be approximated as the area south of a particular latitude and focused on fluxes integrated over the region south of 45°S, noting that the flux products indicate strong meridional gradients and seasonality in the zonal mean fluxes south of 30°S (fig. S18, A and B). We averaged the regional fluxes over individual seasons to regress against the surface mole fraction observations and over 90 days before each aircraft campaign (see SM for sensitivity tests, including an assessment of different region boundaries and a similar analysis based on gradients in total CO_2). There is a robust relationship between the CO_2 flux south of 45°S and $\Delta_\theta CO_2^{ocn}$ across the models (Fig. 3, A and B). The sensitivity of $\Delta_\theta CO_2^{ocn}$ to fluxes varies seasonally, as indicated by a change in slope between seasons. December to February (DJF) is distinct in having a smaller slope (higher sensitivity); the other seasons individually have larger slopes that are similar to each other, thus we grouped data from campaigns flown in March to November together (Fig. 3B). For the surface data, we find a significant positive relationship between the regional air-sea flux and $\Delta_y CO_2$ in DJF across the models (Fig. 3C); the flux-$\Delta_y CO_2$ relationship dwindles in strength during nonsummer months, however, and there is no significant relationship in austral winter [June to August (JJA)] (Fig. 3D). The spread enabling these relationships results from the diversity of flux estimates, while the scatter about the fits represents both different realizations of atmospheric transport and spatiotemporal mismatch between the true surface influence function and our coarse spatiotemporal approximation. The smaller slope for the aircraft data in DJF is consistent with greater atmospheric stability (reduced vertical mixing) over the cold ocean during austral summer, intensifying the flux signal in the lower troposphere; more-energetic vertical mixing in other seasons, as well as stronger horizontal flow, results in diminished sensitivity in $\Delta_\theta CO_2$ and no clear relationship

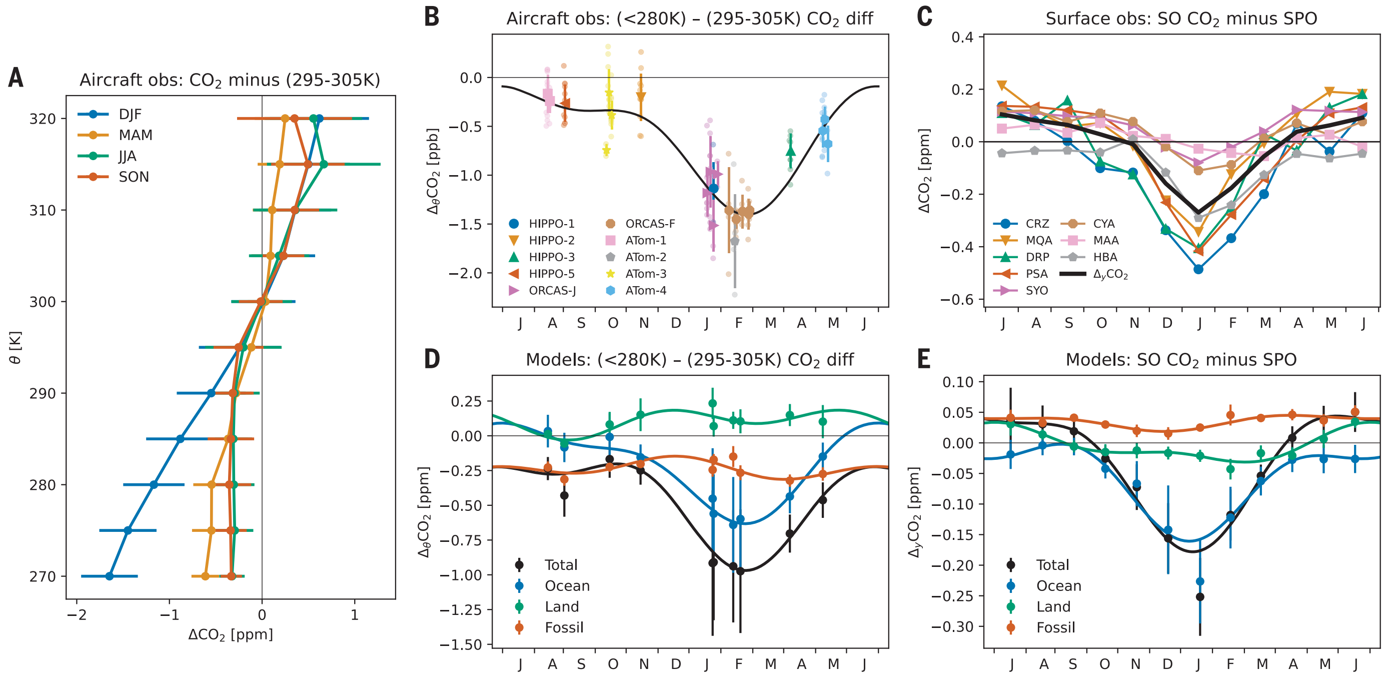

Fig. 2. Seasonal evolution of atmospheric CO_2 over the Southern Ocean. (**A**) Vertical profiles of CO_2 observations collected by aircraft south of 45°S, binned on 5 K potential temperature (θ) bins and averaged by season (whiskers show standard deviation; fig. S6 shows model comparison). MAM, austral fall (March to May); SON, austral spring (September to November). (**B**) The vertical gradient ($\Delta_\theta CO_2$) in CO_2 measured from aircraft south of 45°S. Small points show $\Delta_\theta CO_2$ for individual profiles; larger points show the median and standard deviation (whiskers) for each flight. The black line shows a two-harmonic fit to the flight-median points. (**C**) Monthly climatology (1999–2019) of the latitudinal gradient in CO_2 measured by surface stations (Fig. 1); the black line shows the station mean metric ($\Delta_y CO_2$). Separate laboratory records at Syowa Station (SYO) and Palmer Station (PSA) have been averaged. The seasonal evolution of (**D**) $\Delta_\theta CO_2$ and (**E**) $\Delta_y CO_2$ simulated in a collection of atmospheric inversion models (table S3). The points show the median across the models, and whiskers show the standard deviation. The colors correspond to the total CO_2 (black) and CO_2 tracers responsive to only ocean (blue), land (green), and fossil (red) surface fluxes. Note that the *y* axis bounds differ by panel.

between fluxes and the surface station–based $\Delta_y CO_2$ metric in winter.

Vertical lines in Fig. 3 show representative observations of each gradient metric corrected for land and fossil fuel contributions; the intersection of these lines with the flux-gradient fit provides a quantitative flux estimate. Applying this emergent constraint for each aircraft campaign yields 10 flux estimates spread over 7 months of the year; these data suggest that the Southern Ocean is a strong sink for CO_2 in austral summer, with fluxes that are near-neutral during winter (Fig. 4A). Applying a two-harmonic fit to the data, we estimated an annual mean flux spread over the aircraft observing period (2009–2018) of –0.53 ± 0.23 petagrams of carbon (Pg C) year^{-1} (Fig. 4B). The seasonal cycle of fluxes estimated from aircraft campaigns largely agrees with flux estimates derived from the Surface Ocean CO_2 Atlas (SOCAT) P_{CO_2} data product, using either neural network interpolation (*22*) or the Jena mixed-layer scheme (*23*) (Fig. 4A). Similarly, the aircraft-based fluxes agree with the multimodel mean of inverse estimates, although inversions tend to underestimate summer uptake (fig. S12C), overestimate winter uptake (fig. S12D), and show greater than 100% disagreement on the annual mean flux. We have not explicitly accounted for interannual variability or trends in the fluxes over the period of aircraft data collection (fig. S12, C and D), although we expect this to be a relatively small effect, as seasonal coverage between HIPPO and ATom is relatively uniform (Fig. 4A). The flux estimates obtained from the surface atmospheric CO_2 gradient in summer are consistent with the aircraft-based estimates (fig. S12C) but have larger uncertainty—indeed, the magnitude of the $\Delta_y CO_2$ signal is small relative to analytical uncertainty (SM), a particular challenge in this region, where sites are remote, conditions are harsh, and intercomparison between the multiple laboratories maintaining CO_2 records is limited (*24*, *25*). Despite the large uncertainty, however, trends in $\Delta_y CO_2$ are consistent with increasing Southern Ocean uptake since 2005 (*7*, *26*) (see SM); for instance, $\Delta_y CO_2$ declined by about 0.16 ± 0.03 parts per million (ppm) decade^{-1} over the period 2005–2019 for both DJF and JJA, and while there was no significant flux-gradient relationship in JJA (Fig. 3D), the associated $\Delta_y CO_2$ -based flux estimates suggest the DJF flux was –0.5 ± 0.7 Pg C year^{-1} from 2005 to 2009, –1.1 ± 0.9 Pg C year^{-1} from 2010 to 2014, and –1.3 ± 1.1 Pg C year^{-1} from 2015 to 2019 (fig. S12C). Notably, the aircraft-based flux estimates indicate stronger annual mean uptake than fluxes incorporating P_{CO_2} estimates from the Southern Ocean Carbon and Climate Observations and Modeling (SOCCOM) profiling float pH measurements (*10*, *27*). The primary SOCCOM flux product we examined (SOCAT+SOCCOM) is derived from neural network interpolation including both ship-based surface-ocean P_{CO_2} observations as well as float-derived P_{CO_2} estimates [see SM and (27)]; this product yields weaker annual mean uptake but tracks the individual aircraft campaign flux estimates within uncertainty (Fig. 4A). The other two SOCCOM-based products presented here are sensitivity runs (*10*, *27*) that selectively exclude ship-based P_{CO_2} observations in the Southern Ocean (see SM). While these products have a seasonal phase and amplitude similar to those of the aircraft flux estimates, they indicate greater outgassing in winter and less ingassing during summer than the aircraft-based fluxes (Fig. 4). Such large fluxes should have clear atmospheric signatures

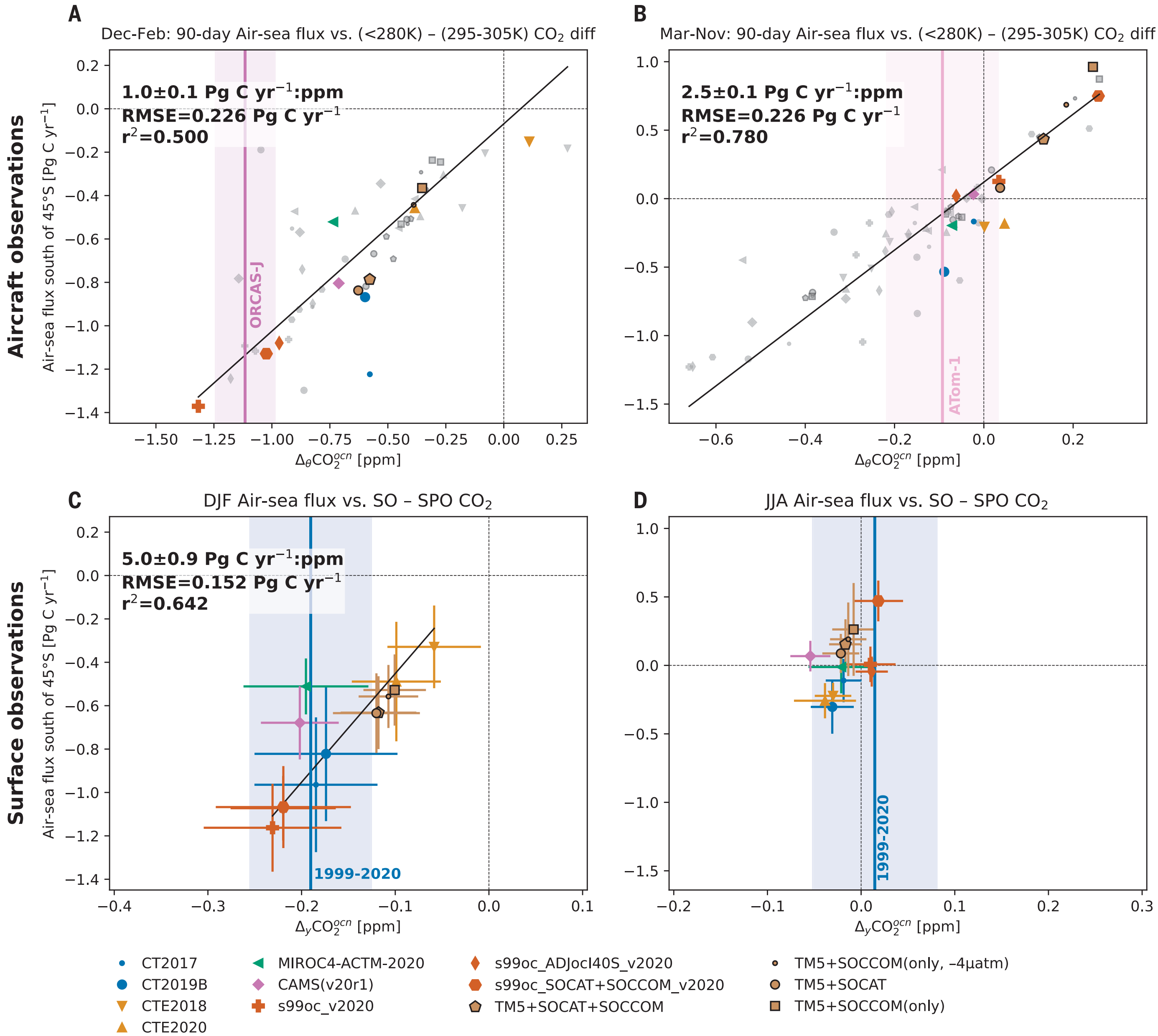

Fig. 3. Emergent constraints on air-sea fluxes south of 45°S. (**A** and **B**) 90 day–mean air-sea fluxes south of 45°S versus $\Delta_\theta CO_2^{ocn}$ from model simulations (see SM) replicating aircraft observations collected during (A) December to February and (B) March to November. Colored vertical lines show an observed value of $\Delta_\theta CO_2$ [ORCAS during January in (A) and ATom-1 in (B)] corrected for land and fossil fuel influence, with shading indicating both analytical uncertainty and model spread in the correction (see SM); colored points highlight the model samples from these particular campaigns, while gray points show data from other campaigns in the (A) December to February or (B) March to November timeframe. Figures S10 and S11 show similar plots for each individual aircraft campaign. (**C** and **D**) Seasonal-mean surface fluxes versus $\Delta_y CO_2^{ocn}$ computed from models for (C) summer (DJF) and (D) winter (JJA) over the period 1999–2019. Points correspond to individual models; whiskers denote the standard deviation of interannual variability. Light blue vertical lines show the observed $\Delta_y CO_2$ corrected for land and fossil fuel influence; shading shows analytical uncertainty and model spread in the correction (see SM; fig. S12, A and B, shows $\Delta_y CO_2$ time series). The sign convention for fluxes is positive upward. Diagonal lines, where significant, show the best-fit line to all data points shown; inset text shows an estimate of the slope with standard error (SM), and goodness-of-fit statistics are also shown. Table S3 provides detailed information on the model products, defining the acronyms used in the legend. Note that the axis bounds differ by panel. See fig. S16 for a version of this plot based on total CO_2.

(Fig. 3, A and B), but no such signatures are evident in any of the Southern Ocean aircraft campaigns (Fig. 2, A and B, and figs. S2, S10, and S11).

Our analysis demonstrates that Southern Ocean air-sea fluxes impart a coherent pattern in atmospheric CO_2 as measured by aircraft. The surface station network is only detectably sensitive to variations in fluxes during austral summer and hampered by measurement noise commensurate with flux signals. Our results highlight the difficulty global atmospheric inversions have in capturing meaningful estimates of Southern Ocean fluxes using existing surface data constraints. It is important to note that a robust emergent constraint (Fig. 3) requires a diverse collection of models to avoid results being affected by biases specific to a single model

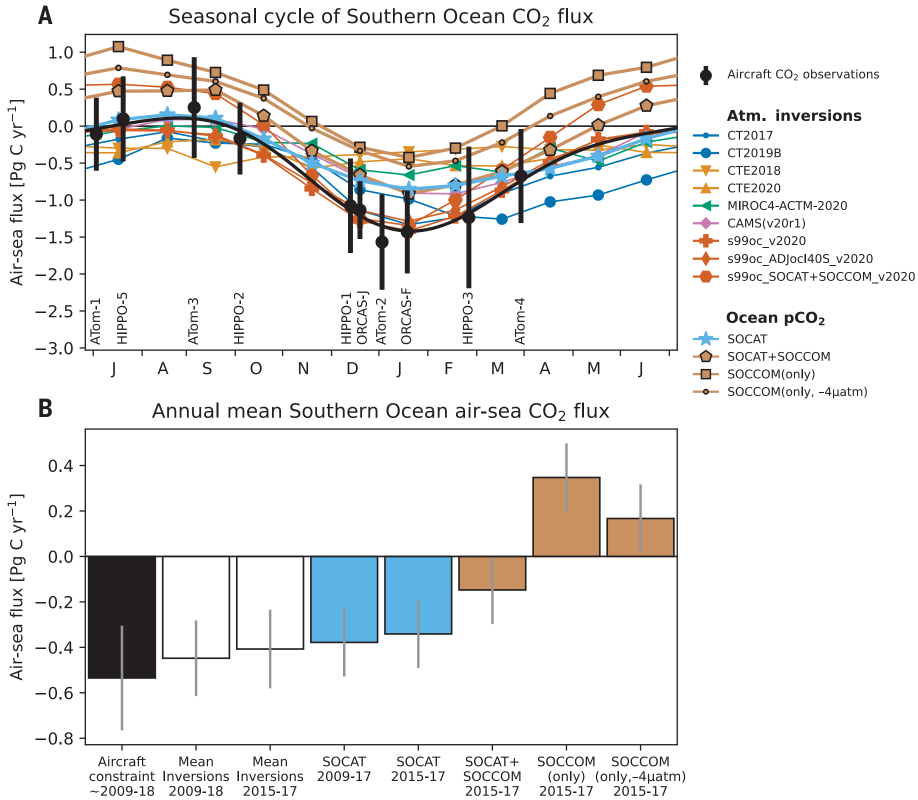

Fig. 4. Observationally based estimates of Southern Ocean air-sea fluxes. (**A**) The seasonal cycle of air-sea CO_2 flux south of 45°S estimated from aircraft campaigns (black points, labels), plotted at the center of the 90-day window for which the emergent flux constraint was calibrated. Whiskers show the standard deviation derived from propagating analytical and statistical uncertainties; the black line shows a two-harmonic fit used to estimate the annual mean flux. The colored lines give the seasonal cycle from atmospheric inversion systems as well as the neural network extrapolation (*22*) of the Surface Ocean CO_2 Atlas (SOCAT) P_{CO_2} observations (*31*) and profiling float observations from the Southern Ocean Carbon and Climate Observations and Modeling (SOCCOM) project (*32*). Fluxes are averaged over the period 2009–2018, except for the three neural network–based flux estimates (*27*) incorporating SOCCOM observations, which are averaged over the period 2015–2017. (**B**) Annual mean flux estimated in this study (leftmost bar) including uncertainty (whisker), along with the mean and standard deviation (whiskers) across the inversion systems shown in (A) as well as the surface-ocean P_{CO_2}-based methods; averaging time periods are noted in the axis labels (both SOCAT flux estimates were derived using neural network training over the full observational period). The uncertainty estimate on the SOCAT and SOCCOM fluxes is approximated from (*10*), which reported ±0.15 Pg C $year^{-1}$ as the "method uncertainty" associated with the neural network–based flux estimates for the whole Southern Ocean (south of 44°S). Note that while s99oc_v2020 and s99c_SOCAT+SOCCOM_v2020 are global inversions, their ocean fluxes are prescribed, not optimized using atmospheric observations (see SM); similarly, the CAMS(v20r1) ocean fluxes remain close to its SOCAT P_{CO_2}-based prior.

or unidentified transport biases common across models. The collection of models we included use four different underlying meteorological reanalysis datasets, four different transport models, and differ in spatial resolution and treatment of vertical transport (table S3); moreover, they make up a substantial proportion of the models commonly used for long-term global CO_2 inversions. However, inclusion of additional model solutions would improve confidence in our result by increasing the number of independent realizations of transport. Despite this potential limitation, aircraft observations leverage the broad integrative power of the atmosphere, which provides an advantage over estimating fluxes from surface ocean P_{CO_2} observations: The ocean surface is heterogeneous, making representative sampling difficult; air-sea fluxes computed from P_{CO_2} estimates depend on an uncertain gas exchange parameterization (*28*); and float-based estimates have additional uncertainty associated with estimating P_{CO_2} itself (*29*). However, we resolved fluxes only over a broadly defined Southern Ocean region; finer-scale spatial features present in surface-ocean P_{CO_2} data can provide important mechanistic insight, reinforcing the need for more high-quality, widely distributed ocean observations to advance process understanding. Uncertainty regarding Southern Ocean carbon uptake is a critical limitation in current understanding of the global carbon cycle (*30*). Our results can be used to validate Earth system models and inversion-based assessments of the Southern Hemisphere carbon budget. Critically, integral constraints on the atmospheric CO_2 budget require balanced fluxes; therefore, our result of strong Southern Ocean uptake alleviates the need to identify missing Southern Hemisphere land or subtropical ocean sinks, as suggested by the float observations. Finally, our analysis has important implications for effective monitoring of the Southern Ocean carbon sink. A regular program of aircraft observations could provide a cost-effective approach to drastically improve estimates of the carbon budget for the Southern Ocean and globally, helping to fulfill a societal requirement for clear understanding of mechanisms driving variation in atmospheric CO_2.

REFERENCES AND NOTES

1. S. Khatiwala, F. Primeau, T. Hall, *Nature* **462**, 346–349 (2009).
2. T. DeVries, *Global Biogeochem. Cycles* **28**, 631–647 (2014).
3. A. Lenton *et al.*, *Biogeosciences* **10**, 4037–4054 (2013).
4. P. Peylin *et al.*, *Biogeosciences* **10**, 6699–6720 (2013).
5. S. Crowell *et al.*, *Atmos. Chem. Phys.* **19**, 9797–9831 (2019).
6. T. Takahashi *et al.*, *Deep Sea Res. Part II Top. Stud. Oceanogr.* **56**, 554–577 (2009).
7. P. Landschützer *et al.*, *Science* **349**, 1221–1224 (2015).
8. N. Gruber *et al.*, *Global Biogeochem. Cycles* **23**, GB1005 (2009).
9. A. R. Gray *et al.*, *Geophys. Res. Lett.* **45**, 9049–9057 (2018).
10. S. M. Bushinsky *et al.*, *Global Biogeochem. Cycles* **33**, 1370–1388 (2019).
11. G. A. McKinley *et al.*, *Nature* **530**, 469–472 (2016).
12. N. Gruber, P. Landschützer, N. S. Lovenduski, *Ann. Rev. Mar. Sci.* **11**, 159–186 (2019).
13. W. Peters *et al.*, *J. Geophys. Res.* **110**, D24304 (2005).
14. I. G. Enting, in *Inverse Methods in Global Biogeochemical Cycles*, P. Kasibhatlaet *al.*, vol. 114 of *Geophysical Monograph Series* (American Geophysical Union, 2000), pp. 19–31.
15. A. S. Denning, I. Y. Fung, D. Randall, *Nature* **376**, 240–243 (1995).
16. A. E. Schuh *et al.*, *Global Biogeochem. Cycles* **33**, 484–500 (2019).
17. S. Basu *et al.*, *Atmos. Chem. Phys.* **18**, 7189–7215 (2018).
18. S. C. Wofsy, *Philos. Trans. R. Soc. A* **369**, 2073–2086 (2011).
19. B. B. Stephens *et al.*, *Bull. Am. Meteorol. Soc.* **99**, 381–402 (2018).
20. S. C. Wofsy *et al.*, ATom: Merged Atmospheric Chemistry, Trace Gases, and Aerosols, version 2, ORNL Distributed Active Archive Center (2021); https://doi.org/10.3334/ORNLDAAC/1925.
21. L. S. Geller *et al.*, *Geophys. Res. Lett.* **24**, 675–678 (1997).
22. P. Landschützer, N. Gruber, D. C. E. Bakker, *Global Biogeochem. Cycles* **30**, 1396–1417 (2016).
23. C. Rödenbeck *et al.*, *Biogeosciences* **11**, 4599–4613 (2014).
24. K. A. Masarie *et al.*, *J. Geophys. Res.* **106**, 20445–20464 (2001).
25. R. J. Francey, J. S. Frederiksen, L. P. Steele, R. L. Langenfelds, *Atmos. Chem. Phys.* **19**, 14741–14754 (2019).
26. D. R. Munro *et al.*, *Geophys. Res. Lett.* **42**, 7623–7630 (2015).
27. P. Landschützer, S. M. Bushinsky, A. R. Gray, A combined globally mapped carbon dioxide (CO_2) flux estimate based on the Surface Ocean CO_2 Atlas Database (SOCAT) and Southern Ocean Carbon and Climate Observations and Modeling

(SOCCOM) biogeochemistry floats from 1982 to 2017 (NCEI Accession 0191304), NOAA National Centers for Environmental Information (NCEI) (2019); https://doi.org/10.25921/9hsn-xq82.
28. R. Wanninkhof, *Limnol. Oceanogr. Methods* **12**, 351–362 (2014).
29. N. L. Williams *et al*., *Global Biogeochem. Cycles* **31**, 591–604 (2017).
30. J. G. Canadell *et al*., in *Climate Change 2021: The Physical Science Basis. Contribution of Working Group I to the Sixth Assessment Report of the Intergovernmental Panel on Climate Change*, V. Masson-Delmotte *et al*., (Cambridge Univ. Press, 2021), chap. 5.
31. D. C. E. Bakker *et al*., *Earth Syst. Sci. Data* **6**, 69–90 (2014).
32. K. S. Johnson *et al*., *J. Geophys. Res. Oceans* **122**, 6416–6436 (2017).
33. UCAR/NCAR - Earth Observing Laboratory, NSF/NCAR GV HIAPER Aircraft (2005); https://doi.org/10.5065/D6DR2SJP.
34. S. C. Wofsy *et al*., HIPPO Merged 10-Second Meteorology, Atmospheric Chemistry, and Aerosol Data, version 1.0, UCAR/NCAR - Earth Observing Laboratory (2017); https://doi.org/10.3334/CDIAC/HIPPO_010.
35. S. Wofsy *et al*., HIPPO NOAA Flask Sample GHG, Halocarbon, and Hydrocarbon Data, version 1.0, UCAR/NCAR - Earth Observing Laboratory (2017); https://doi.org/10.3334/CDIAC/HIPPO_013.
36. S. Wofsy *et al*., HIPPO MEDUSA Flask Sample Trace Gas and Isotope Data, version 1.0, UCAR/NCAR - Earth Observing Laboratory (2017); https://doi.org/10.3334/CDIAC/HIPPO_014.
37. B. Stephens, ORCAS Merge Products, version 1.0, UCAR/NCAR - Earth Observing Laboratory (2017); https://doi.org/10.5065/D6SB445X.
38. M. C. Long *et al*., Southern Ocean Air-Sea Carbon Fluxes from Aircraft Observations: Modeling Datasets, version 1.0, UCAR/NCAR - DASH Repository (2021); https://doi.org/10.5065/fepv-0z52.
39. M. C. Long, B. B. Stephens, Southern Ocean Air-Sea Carbon Fluxes from Aircraft Observations: Analysis code, National Center for Atmospheric Research (2021);https:/doi.org/10.5065/6vnv-1x08.

ACKNOWLEDGMENTS

Many people contributed to the collection of data used in this study. We thank R. Jimenez, J. Pittman, S. Park, B. Xiang, G. Santoni, M. Smith, and J. Budney for HIPPO and ATom Harvard QCLS and OMS CO_2 data; T. Newberger, F. Moore, and G. Diskin for ORCAS and ATom NOAA Picarro and PFP CO_2 data; A. Watt, S. Shertz, B. Paplawsky, and S. Afshar for HIPPO, ORCAS, and ATom NCAR AO2 and NCAR/Scripps Medusa CO_2 data; J. Elkins, F. Moore, and E. Hintsa for ATom-1 N_2O data; R.-S. Gao and R. Spackman for HIPPO O_3 data; T. Ryerson, J. Peischl, I. Bourgeois, and C. Thompson for ATom O_3 data; M. Zondlo, M. Diao, and S. Beaton for HIPPO and ORCAS H_2O data; and G. Diskin and J. DiGangi for ATom H_2O data. We thank the flight crew and support staff for the NSF/NCAR GV (*33*), which is part of NSF's Lower Atmosphere Observing Facilities, and the NASA DC-8, which is supported by the NASA Airborne Science Program and Earth Science Project Office. We thank the institutions and investigators responsible for the surface station records used in the study, including NOAA, CSIRO, Scripps, NIWA, SAWS, Program 416 from the French Polar Institute (IPEV), Tohoku University, and National Institute of Polar Research (NIPR), and in particular E. Dlugokencky, R. Langenfelds, S. Walker, G. Brailsford, S. Nichol, C. Labuschagne, W. Joubert, and S. Morimoto. We thank K. Lindsay, J.-F. Lamarque, and F. Vitt for useful modeling discussions. We thank R. Wanninkhof and two anonymous reviewers for their comments that improved this manuscript. CarbonTracker (CT2017, CT2019B) results provided by NOAA ESRL, Boulder, Colorado, USA, from the website http://carbontracker.noaa.gov. We thank A. Jacobson for the TM5 transport simulations. We thank the SOCAT and SOCCOM science teams and specifically P. Landschützer, S. Bushinsky, and A. Gray for providing flux estimates. **Funding:** This material is based on work supported by the National Center for Atmospheric Research, which is a major facility sponsored by the NSF under Cooperative Agreement No. 1852977. Computing resources were provided by the Climate Simulation Laboratory at NCAR's Computational and Information Systems Laboratory (CISL). Data were collected using NSF's Lower Atmosphere Observing Facilities, which are managed and operated by NCAR's Earth Observing Laboratory. Additional sources of funding include NSF-PLR-1502301, NSF-ATM-0628388, NSF-ATM-0628519, NSF-ATM-0628575, NSF-PLR-1501993, NSF-PLR-1501292, NSF-PLR-1501997, NSF-AGS-1547626, NSF-AGS-1547797, NSF-AGS-1623745, NSF-AGS-1623748, NASA-NNX17AE74G, NASA-NNX15AJ23G, NASA-NNX16AL92A, and NOAA-NA15OAR4320071. **Author contributions:** M.C.L., B.B.S., K.M., and C.S. conceived of the study. B.B.S., E.J.M., J.D.B., R.F.K., E.A.K., B.C.D., R.C., S.C.W., K.M., C.S., P.T., A.S., Z.L., P.B.K., M.R., and D.M. collected and helped interpret CO_2 observational data. C.R., N.C., P.P., F.C., I.T.L., and W.P. produced and helped interpret model output. M.C.L. and B.B.S. performed the analysis and wrote the paper. All authors contributed to interpretation of the results and provided feedback on the manuscript. **Competing interests:** The authors declare no competing interests. **Data and materials availability:** Links providing access to the surface observational datasets used in this study are available in table S1; the aircraft data are available in references for HIPPO (*34–36*), ORCAS (*37*), and ATom (*20*). All model data are available via the UCAR/NCAR - Digital Asset Services Hub (DASH) Repository (*38*). Code to reproduce this calculation is documented and accessible (*39*).

SUPPLEMENTARY MATERIALS

science.org/doi/10.1126/science.abi4355
Materials and Methods
Supplementary Text
Figs. S1 to S19
Tables S1 to S4
References (*40–83*)

9 March 2021; accepted 18 October 2021
10.1126/science.abi4355

Science

Strong Southern Ocean carbon uptake evident in airborne observations

Matthew C. LongBritton B. StephensKathryn McKainColm SweeneyRalph F. KeelingEric A. KortEric J. MorganJonathan D. BentNaveen ChandraFrederic ChevallierRóisín CommaneBruce C. DaubePaul B. KrummelZoë LohIngrid T. LuijkxDavid MunroPrabir PatraWouter PetersMichel RamonetChristian RödenbeckAnn StavertPieter TansSteven C. Wofsy

Science, 374 (6572), • DOI: 10.1126/science.abi4355

Up in the air
Understanding ocean-atmospheric carbon dioxide (CO) fluxes in the Southern Ocean is necessary for quantifying the global CO budget, but measurements in the harsh conditions there make collecting good data difficult, so a quantitative picture still is out of reach. Long *et al*. present measurements of atmospheric CO concentrations made by aircraft and show that the annual net flux of carbon into the ocean south of 45°S is large, with stronger summertime uptake and less wintertime outgassing than other recent observations have indicated. —HJS

Science (ISSN) is published by the American Association for the Advancement of Science. 1200 New York Avenue NW, Washington, DC 20005. The title *Science* is a registered trademark of AAAS.